Journal of Nonlinear Waves (2026), **xx**:xx 1–22

CAMBRIDGE
UNIVERSITY PRESS

RESEARCH ARTICLE

Soliton stabilization on top of a hill: a nonlinear-wave inverted pendulum

Roberto Marquez[1,2], Paul Belinsky[1] and R. Carretero-González[1,3]

[1] Nonlinear Dynamical Systems Group, Department of Mathematics and Statistics, San Diego State University, San Diego, 92182-7720, CA, USA .
[2] Department of Aerospace Engineering, San Diego State University, San Diego, 92182-1308, CA, USA .
[3] Computational Science Research Center, San Diego State University, San Diego, 92182-1245, CA, USA .

Keywords: solitons; nonlinear Schrödinger equation; inverted pendulum; Mathieu equation

Abstract
We construct a nonlinear-wave analogue of the celebrated inverted, Kapitza, pendulum. We consider bright soliton solutions of the one-dimensional nonlinear Schrödinger (NLS) equation under the influence of a repelling, when stationary, hump (or "hill") potential and a confining harmonic trap. Using the variational approximation methodology, we reduce the soliton dynamics to an effective Newton-type model on the soliton position and study its behavior when the hump potential is made to vibrate vertically. We corroborate that the effective model is able to qualitatively and quantitatively describe the statics, stability, and dynamical properties of the original NLS bright soliton. Using the effective model, we find the stability regions as a function of the hump parameters (height and vertical shaking frequency) which correspond to the stability tongues of the Mathieu equation. We show that these theoretically predicted regions accurately describe the corresponding, numerically computed, Floquet stability regions of the original soliton on top of the vertically vibrating hill. Inside these stability regions we are able to fully stabilize the soliton on top of the hill as a result of the vertical shaking in a manner akin to the inverted, Kapitza, pendulum.

1. Introduction

In this work we focus on the nonlinear Schrödinger (NLS) equation under the effects of external potentials which is also known as the Gross-Pitaevskii (GP) equation in the realm of atomic and molecular physics. This quintessential model, being the lowest order nonlinear partial differential equation (PDE) describing the evolution of envelope waves in a nonlinear medium, finds its application in a wide range of physical systems [13]. Particularly interesting are the applications of the NLS/GP equation to nonlinear optics [3] and Bose-Einstein condensates (BECs) [54, 65, 30]. In both of these applications, the incorporation of an external potential, which can naturally be made time-dependent, allows for the direct manipulation of the coherent structures supported in these nonlinear media owing to the balance between nonlinearity and dispersion.

For instance, in nonlinear optical media supporting optical solitons [33] it is possible to replace passive propagation by control through engineered external potentials, including non-autonomous linear and harmonic potentials to manipulate the soliton's position and shape parameters [61] and transverse refractive-index landscapes and longitudinally modulated photonic lattices enabling soliton switching, steering, mobility control, and reshaping [20, 58, 28]. More recently, control has been extended to Floquet and topological photonic platforms [47], including nonlinear unidirectional edge states [48], and period-doubled Floquet solitons [49]. Current developments also include dissipative Kerr soliton-comb states in Floquet topological systems [21] and programmable manipulation of temporal solitons in recirculating fiber loops using synthetic external potentials [15]. Particularly interesting is the optical trapping and manipulation of pulses for information processing [38, 5]. The so-called temporal tweezing offers an efficient method to store and reconfigure optical information. For instance, soliton transfer has been achieved in continuum and discrete media [53] and periodic time-dependent [31, 55] or radial-Bessel [22] lattices external potentials have been used to manipulate solitons. Finally, the tweezing of cavity solitons in media with strong gain and loss has also been studied [24, 59].

On the other hand, within the realm of BECs, matter-wave solitons provide a particularly direct route for studying coherent nonlinear excitations under external control. In what concern solitons, dark solitons in repulsive condensates were experimentally generated by phase imprinting [6], while, more relevant to our current presentation, bright solitons and soliton trains in attractive condensates have been observed in quasi-1D potentials [32, 64]. The use of external potentials has become central to both the theory and control of these coherent structures. Slowly varying harmonic traps have been used to determine soliton trajectories and oscillation frequencies [7], while expulsive and waveguide geometries have been used to guide bright solitons and control their emissions [12]. Subsequent work generalized the manipulation paradigm to the so-called dark-bright complexes in multicomponent, spinor, BECs by using spatially or temporally varying external potentials providing an effective platform for steering, stabilizing, and manipulating solitons [19, 29]. Particularly relevant to our present work is the manipulation of bright matter-wave solitons in 1D geometries based on external potentials protocols. Some of these applications include the use of expulsive and waveguide potentials as mechanisms for stabilizing, emitting, and destabilizing bright solitons [12] and combined harmonic traps and optical lattices were used theoretically to pin, move, and manipulate bright solitons through effective potential landscapes [60]. Importantly, bright solitons have become a platform for coherent atom-optical devices: solitonic interferometry has been realized using Bragg pulses from an optical lattice in a waveguide [42], and barrier-based splitting, reflection, recombination, and scattering have been developed as routes to precision sensing and controlled soliton transport. These efforts advocate for the use of bright BEC solitons not merely as self-trapped wave packets, but as programmable nonlinear matter-wave objects whose center-of-mass motion, internal breathing, collisions, phase relations, and interferometric response can be engineered using time-dependent external potentials including multicomponent and spin-orbit-coupled settings [68, 29].

In this work we consider the effects of a repulsive hump or “hill” potential on the dynamics of a bright soliton. In the case of a *static* repulsive hump, the soliton is endemically unstable along the translational (sliding) mode which is responsible for a soliton starting at the top of the hill to eventually slide down along one of the hill sides. However, if one introduces a well-crafted vertical periodic oscillation of the hump height, we will show that it is possible to completely stabilize the soliton on top of the hill. The mechanism behind this stabilization is same as the celebrated inverted, or Kapitza, pendulum. The Kapitza, or dynamically stabilized inverted, pendulum is one of the classical paradigms showing that a rapidly driven system can acquire stable equilibria that are absent in the corresponding static problem. The essential observation predates Kapitza: Stephenson showed in 1908 that vertical vibration of the point of suspension can induce stability of the otherwise unstable upright pendulum [63]. Kapitza later gave the now-standard physical and analytical explanation, demonstrating that, for appropriate system parameter combinations (namely, sufficiently rapid vertical oscillations of the pivot), the pendulum exhibits an effective time-averaged potential with a local *minimum* at the inverted position [26, 27]. Later studies clarified the nonlinear stability domains, bifurcations, fractal basins, and loss of stability of the inverted state under finite-frequency forcing [4], while pedagogical and analytical treatments have emphasized the physical mechanism and the limits of the usual high-frequency stabilization criterion [8, 9]. More recently, the same idea has been generalized beyond a single rigid pendulum to microscopic, quantum, many-body, and engineered systems, where rapid modulation can reshape effective Hamiltonians and stabilize otherwise unstable states [57, 14]. The Kapitza pendulum is a canonical example of parametric stabilization and it remains a standard model for averaging theory, Floquet studies, nonlinear stability, and control. Thus, the Kapitza pendulum serves not only as historical mechanical curiosity, but as a prototype for dynamical stabilization by periodic forcing.

This manuscript is organized as follows. In Sec. 2 we introduce the system that we will study. Namely, within the auspices of the NLS equation, we study the dynamics and stability of a bright soliton on top of a *stationary*, repelling, hump. Then, in Sec. 3, using the variational approximation methodology, we cast a reduced Newton-type effective model on the soliton position that is able to accurately describe the statics and dynamics of the bright soliton under the presence of a vertically shaking hump and a confining parabolic trap. In Sec. 4 we leverage the results of the Mathieu equation for the stabilization of the reduced effective model under the presence of vertical shaking of the hump potential. This, in turn, allows us to find parameter regions of our initial NLS model where the soliton on top of the hill is completely stabilized by the periodic hump forcing in a manner akin to the Kapitza pendulum. Finally, in Sec. 5 we summarize our results and put forward some avenues for possible related, future, investigations.

2. Bright solitons on top of a hill

2.1. The nonlinear Schrödinger (NLS) equation

To study the manipulation of bright solitons in nonlinear media we will focus on the normal-form PDE for propagation of envelope waves in nonlinear media: the NLS or GP equation [13]. The most basic form for this nonlinear PDE in 1D may be cast, after suitable adimensionalization [13], as follows:

$$iu_t = -\frac{1}{2}u_{xx} - |u|^2u + Vu, \tag{2.1}$$

where the complex field $u(x,t)$ represents the wavefunction for the system while the potential $V(x,t)$ may be, in general, a function of space x and time t. In actual atomic and optical experiments the usual observable is $|u|^2$ which corresponds, respectively, to the density of atoms or the optical power. In this work we fix the sign in front of the (cubic) nonlinear term to be negative, which corresponds to an attractive (focusing) nonlinearity in the realm of BECs (optics). In the absence of external potential effects [$V(x,t) = 0$], the NLS equation (2.1) supports exact bright solitons solutions whose general form is given by:

$$u(x,t) = A\,\mathrm{sech}\left(A(x-ct-x_0)\right)\exp\left(icx + i\frac{A^2-c^2}{2}t\right), \tag{2.2}$$

where A is the amplitude and (inverse) width of a soliton travelling at constant speed c and initial position x_0.

We now focus on the dynamics of bright solitons under the effects of an external potential that is the combination of a confining parabolic trap and a *repulsive* hump of the form:

$$\begin{aligned} V(x,t) &= V_{\mathrm{MT}}(x) + V_H(x,t) \\ &= \frac{1}{2}\Omega^2x^2 + H(t)\,\mathrm{sech}^2(Bx), \end{aligned} \tag{2.3}$$

where V_{MT} correspond to a parabolic confinement of strength Ω while V_H corresponds to a localized "hump" potential with, in general, time-dependent amplitude $H(t)$ and fixed (inverse) width B. In BEC experiments, the parabolic trapping is typically incorporated through the application of a magnetic potential while the hump potential can be naturally achieved, and precisely controlled, through a blue-detuned external optical (laser) barrier [67, 23]. It is also relevant to note that our potential corresponds to a double-well potential that can also be achieved using the competition between a (positive) quartic term and a (negative) quadratic one (see for instance Refs. [16, 18, 25] and references therein). The temporal forcing due to the hump potential will be determined by the following periodic vertical shaking profile:

$$H(t) = H_0 + \Delta \cos(\omega t), \tag{2.4}$$

where the nominal height of the potential hump is denoted by H_0, and Δ and ω are, respectively, the amplitude and frequency of the periodic shaking off of the nominal height. Note that we will consider a *repulsive* hump such that $H_0 > 0$ and we will try to maintain $\Delta < H_0$ so that the hump always presents a repulsive term for the bright soliton.

The main question that this work tackles is whether a soliton sitting on top of the hill can be stabilized under an appropriate periodic forcing [given by $H(t)$] in a manner akin to the stabilization of the forced inverted pendulum, the so-called Kapitza pendulum [26, 27]. In fact, it has been shown that a bright soliton on top of an *expulsive* parabolic potential can be stabilized by an appropriate periodic variation of the potential strength [1] or the strength of the nonlinearity (i.e., the scattering length) [37]. The ultimate mechanism responsible for this stabilization in the (originally, when no vibration is introduced) expulsive potential is the same that in our current work. Namely, after linearization, the resulting dominant dynamical variable (i.e., the position of the soliton) is described by the parametric stability regions of a Mathieu-type ordinary differential equation (ODE). It is also worth mentioning that the Kapitza stabilization mechanism can also be used to stabilize solutions (which are endemically unstable in a homogeneous in space and time setup) through the periodic modulation of the nonlinear term. See for instance Ref. [46], and references therein, for the stabilization of 2D NLS Townes solitons by an appropriate periodic modulation of the corresponding cubic term.

2.2. Soliton's statics, stability, and eigenmodes

Let us first describe the bright soliton steady states and their stability in the absence of the periodic perturbation, namely when $\Delta = 0$. In this *static* case, the potential (2.3) reduces to the time-independent potential $V(x) = \frac{1}{2}\Omega^2 x^2 + H_0 \,\mathrm{sech}^2(Bx)$. As we are considering $H_0 > 0$, $V(x)$ corresponds to, for strong enough values of H_0, a bistable potential as depicted by the green curve in panel (a) of Fig. 1. The bistability allows for the existence of two solution types: (i) an unstable solution at the top of the hill ($x = 0$) [see dotted red curve in panel (a)] and (ii) a pair of solutions symmetric about $x = 0$ [see blue curve in panel (a)]. The position of the stable solutions is not of great importance here as we will consider soliton solutions near $x = 0$. Nonetheless, it is possible to estimate these stable positions using the variational approximation presented below in Sec. 3. Stationary solutions are obtained for the steady-state profile $w(x)$ by replacing $u(x,t) = w(x)\exp(-i\mu t)$ in Eq. (2.1) where μ corresponds to the so-called chemical potential in the context of BECs or the (negative of) the temporal frequency in the context of optics. Steady states are thus solutions of the stationary problem:

$$-\frac{1}{2}w_{xx} - |w|^2 w + [V(x) - \mu]w = 0.$$

In all numerical results we employ standard finite difference schemes in space to approximate the second spatial derivatives. Steady states are then numerically found by using standard Newton iterations (see Sec. 22.2 in Ref. [13]), until machine precision is achieved, starting with the analytical solution in the absence of external potential ($V = 0$) given in Eq. (2.2) where $\mu = -A^2/2$ (since $c = 0$ in this stationary case). Specifically, for the spatial discretization we used a second order central difference scheme on the interval $x \in [-15, 15]$ with $N_x = 301$ mesh points and (zero) Dirichlet boundary conditions. We checked that finer discretizations did not significantly alter the results. In regards to the time integration for the dynamics, we used a standard fourth order Runge-Kutta method and, in order to ensure numerical stability, we chose the time-step to be half of the threshold time-step given in Ref. [11].

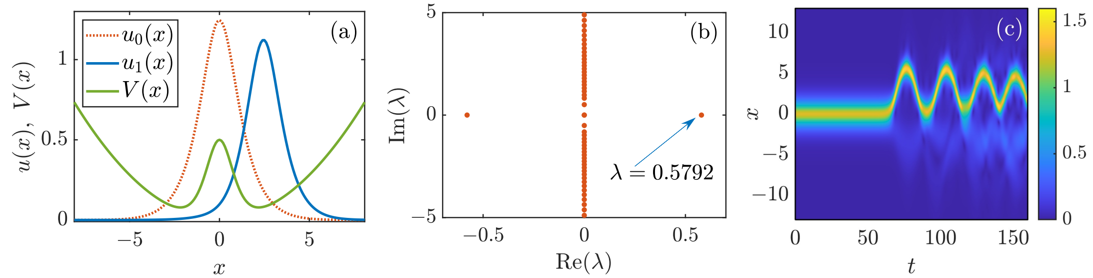

Figure 1. *(Color online) Statics, stability, and dynamics for a bright soliton inside the bistable potential consisting of a harmonic trap and a repelling central hump. (a) The potential (green curve), corresponding to* $\Delta = 0$*,* $\Omega = 0.15$*, and* $H_0 = 0.5$*, supports unstable* u_0 *(red dotted curve) and stable* u_1 *(blue curve) solitons. Both solutions were obtained for* $\mu = -1/2$*. (b) Stability spectrum for the unstable bright soliton on top of the hill. (c) Typical dynamical destabilization of the soliton on top of the hill when adding a small random perturbation of size* 10^{-6}*. Shown is* $|u|$ *as a function of space-time* (x, t)*.*

As concerns the stability of stationary ($\Delta = 0$) bright solitons at the top of the hill ($x = 0$), we cast the linear perturbation off of the steady state $w(x)$ using the ansatz $u(x,t) = [w(x) + \epsilon\, p(x,t)]\, e^{-i\mu t}$ with perturbation $p(x,t) = a(x)e^{\lambda t} + b(x)e^{\lambda^* t}$ and corresponding eigenvalue λ and eigenfunction $\mathcal{W} = (a, b^*)^T$ where the asterisk denotes complex conjugate and $(\cdot)^T$ denotes the transpose. This linear perturbation yields the so-called Bogoliubov-de-Gennes (BdG) equations, namely the eigenvalue problem (see Chap. 22.2 in Ref. [13] for more details):

$$iM\mathcal{W} = i\begin{pmatrix} M_{11} & M_{12} \\ M_{21} & M_{22} \end{pmatrix}\mathcal{W} = \lambda\mathcal{W},$$

where the matrix operator M is composed by the blocks:

$$M_{11} = \frac{1}{2}\partial_{xx} - \left(2g|w|^2 + V - \mu\right), \quad M_{12} = -g\, w^2, \quad M_{22} = -M_{11}^*, \quad M_{21} = -M_{12}^*.$$

To numerically compute the stability spectra we again recur to standard second order finite differences in space to cast the continuum BdG into its discrete counterpart. Panel (b) in Fig. 1 shows a typical example of the stability spectrum for the soliton on top of the hill for a relatively weak hump height. In this case, the system admits a single eigenvalue pair of unstable eigenvalues that corresponds to the instability of the translational mode. This translational mode, or *sliding* mode as we call it from now on, is responsible for the destabilization of the soliton that eventually slides down the hill as shown in panel (c) of Fig. 1. As we will explain now, it should be noted that, for larger hump heights, there exist another pair of unstable eigenvalues corresponding to the splitting mode of the soliton responsible for “rupturing” the soliton into two equal packets on each side of the hump.

We now systematically extract the most unstable eigenvalues for the soliton on top of the hill as the system parameters are varied. Specifically, we fix $\mu = -1/2$ (corresponding to a soliton of height $A = 1$ in the absence of any potential effects) and vary the harmonic trap strength Ω and the hump height H_0. The corresponding results are depicted in Fig. 2. The top panels correspond to the variation of the sliding (solid curves) and splitting (dotted curves) mode eigenvalues as a function of the hump strength in the absence [see panel (a)] and in the presence [see panel (b)] of the parabolic trapping. As it can be seen from this stability spectra, in the absence of the magnetic trap ($\Omega = 0$) the sliding mode becomes unstable (its real part [solid blue curve]) as soon as the hump potential is turned on. Then, for a larger value of the hump strength, a secondary bifurcation is responsible for the splitting mode

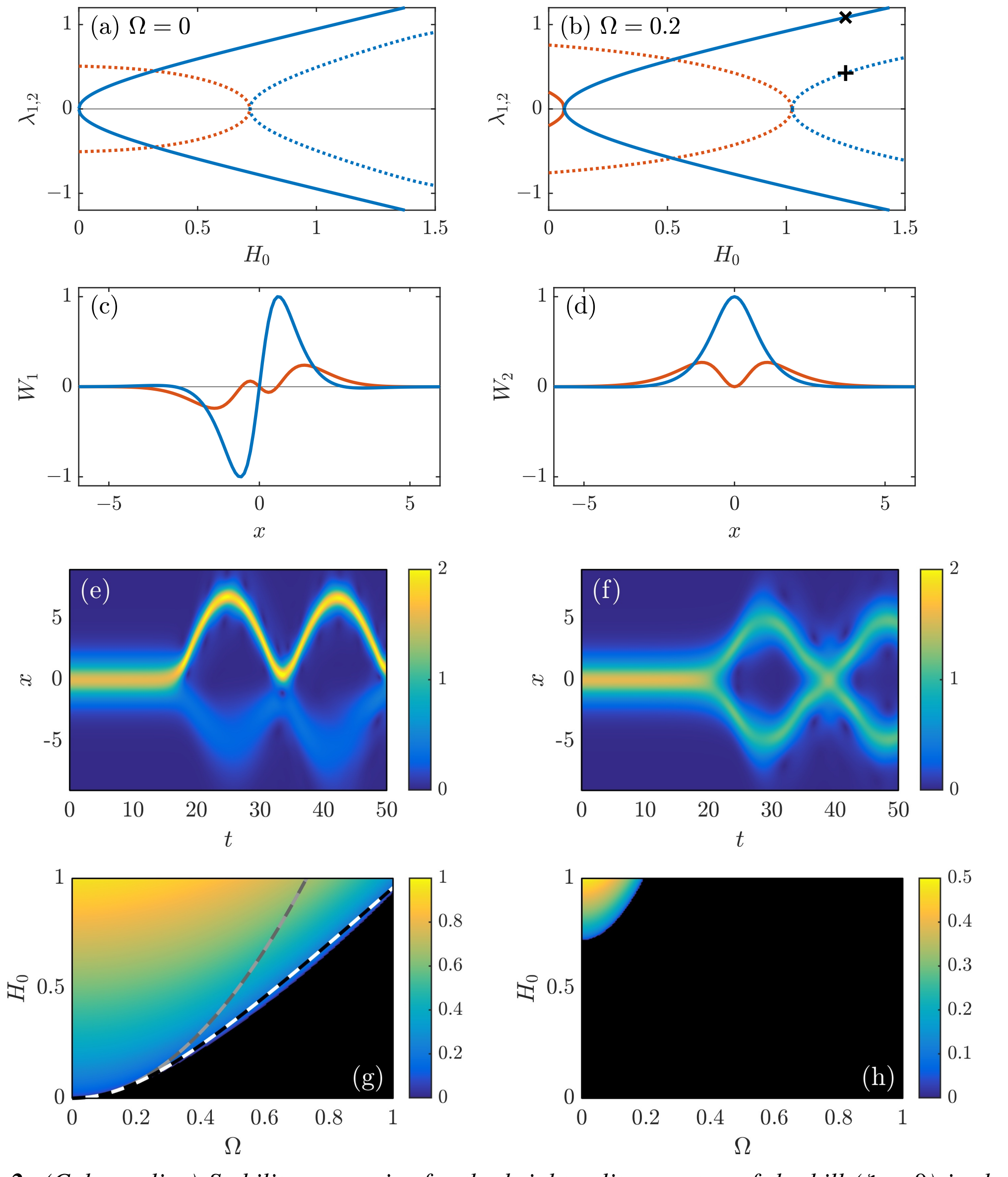

Figure 2. *(Color online) Stability properties for the bright soliton on top of the hill ($\xi = 0$) in the absence of the vertical shaking ($\Delta = 0$) and for $\mu = -1/2$. The top row of panels shows the stability eigenvalues associated with the (translational) sliding (see solid curves) and splitting (see dotted curves) modes for two different values of the magnetic trapping strength Ω as a function of the hump height (H_0). Real and imaginary parts are depicted, respectively in blue and red. The second row of panels depicts the (c) sliding and (d) splitting eigenmodes (real and imaginary parts depicted, respectively, in blue and red) for $\Omega = 0.2$ and $H_0 = 1.25$ [see, respectively, the cross and plus symbols in panel (b)]. The third row of panels depicts the destabilization dynamics after slightly (10^{-5}) perturbing the steady state with the (e) sliding and (f) splitting modes for $\Omega = 0.2$ and $H_0 = 1.25$. The bottom set of panels depicts the two largest instabilities [(g) Re(λ_1): sliding and (h) Re(λ_2): splitting] in the (Ω, H_0) plane. Darker colors correspond to less unstable conditions and black corresponds to complete stabilization. The dashed curves depict the theoretical predictions from the effective ODE model as per Eq. (4.4) with (black and white) and without (grey) the soliton height improvement.*

(dotted curve) to become unstable. In contrast, when the magnetic trap is turned on ($\Omega > 0$), there is a region for relatively small values of the hump height where the sliding mode is stable. Then, for larger values of the hump height the sliding mode becomes unstable and, for even larger hump heights, the splitting mode also becomes unstable. The overall qualitative effect of the magnetic trap is to "shift" the spectrum to the right and to widen the stability regions as the trap is stronger. Panels (c) and (d) depict, respectively, the sliding and splitting modes for $\Omega = 0.2$ and $H_0 = 1.25$ [see the black cross and plus symbols in panel (b) depicting their respective (unstable) eigenvalues]. Panel (e) and (f) show how these unstable modes manifest themselves in the dynamics of the destabilization of the soliton on top of the hill. For the sliding mode [see panel (e)], the instability eventually forces the soliton to slide down the hump and then perform oscillations about the potential minimum. Note that due to radiation effects (see visible lighter blue areas about the main soliton path in yellow), the soliton does have enough energy to come back to its original starting location ($x = 0$). On the other hand, when the soliton is perturbed by the unstable splitting mode, it eventually destabilizes by breaking into two symmetric blobs that slide down over each side of the hump. After their initial sliding, the two blobs perform oscillation and regroup back close to $x = 0$ but, again due to radiation loss, the initial condition on top of the hill is not fully recovered. Finally, we depict in panels (g) and (h) the dependence of the destabilization rates (i.e., real part of the eigenvalues) for, respectively, the sliding and splitting modes as a function of the trap strength Ω and the hump height H_0 (black regions correspond to stable choices for the parameters). Note that for all combinations of (Ω, H_0), the sliding mode is always dominant. Thus, unless one carefully crafts an initial condition that only perturbs along the splitting mode without affecting the sliding mode [precisely as it was done in panel (f)], a typical (random) perturbation will generically destabilize along the sliding mode. This is important in what follows as we are aiming to stabilize the soliton on top of the hill with a periodic perturbation of the hump height in a manner akin to the inverted pendulum. Therefore, we need to primarily focus on taming this sliding mode if we have any hope of achieving such stabilization. As we will see below, in the regions of stabilization of the sliding mode, we were not able to detect destabilization due to the splitting mode and, therefore, we will be able to *fully stabilize* the soliton on top of the hill.

3. Dynamical reduction of the soliton's dynamics

Let us now deploy a reduced model that, not only qualitatively but also quantitatively (in appropriate parameter regions), reproduces the dynamics of the bright soliton as it slides along the hump potential. For that purpose, we deploy the variational approximation (VA) formalism [40] (see also Chap. 25 in Ref. [13] and references therein). As a preliminary disclaimer, we are going to cast the *simplest* possible reduced model by using the least amount of variational parameters that can still capture (qualitatively and quantitatively) the statics, dynamics, and stability of the soliton under the periodic forcing exerted by the vertically vibrating hump. Nonetheless, we will check that our results do give qualitative and, more importantly, quantitative information about the parameter combinations that allow for the full stabilization of the bright soliton on top of the hill thanks to the effect of the periodic perturbation of the hump's height.

Proceeding with the standard VA formalism, the NLS (2.1) can be cast by extremizing the action of the Lagrangian density given by:

$$\mathcal{L}[u] = \frac{i}{2}(u^* u_t - u u_t^*) - \frac{1}{2}|u_x|^2 - \frac{1}{2}|u|^4 - V(x,t)|u|^2. \tag{3.1}$$

We then restrict our attention to the following bright soliton ansatz:

$$u_a(x,t) = A\operatorname{sech}(A(x - \xi(t)))\exp(iv(t)x), \tag{3.2}$$

where A is the *fixed* amplitude and (inverse) width of the soliton while $\xi(t)$ and $v(t)$ are the variational parameters corresponding, respectively, to the position and velocity of the soliton. It is important to stress that we are fixing the soliton amplitude and (inverse) width (namely, they are *not* variational parameters) and the only variational parameters are the position and velocity of the soliton. Then, using the external potential as the combination of the confining parabolic and the repelling hump potential of Eq. (2.3), it is possible to evaluate the Lagrangian density (3.1) on the soliton ansatz (3.2) and integrate all over space to obtain the effective Lagrangian:

$$\begin{aligned}\mathcal{L}_a &= \int_{-\infty}^{\infty} \mathcal{L}[u_a(x,t)]\,dx \\ &= -\frac{2A}{B}\dot{v}(t)\,\xi(t) - \frac{A^2B}{3} - \frac{A^2}{B}v(t)^2 + \frac{2A^4}{3B} - \frac{A^2\Omega^2\left(12B^2\xi(t)^2+\pi^2\right)}{12B^3} - I(x,t),\end{aligned}$$

where $I(x,t)$ is the overlapping integral between the hump potential and the soliton shape:

$$I(x,t) \equiv \int_{-\infty}^{+\infty} V_H\,|u_a|^2\,dx = A^2H(t)\int_{-\infty}^{+\infty} \operatorname{sech}^2(Bx)\operatorname{sech}^2(A(x-\xi))\,dx. \tag{3.3}$$

Unfortunately, close form expressions for $I(x,t)$ are only available when the soliton width (A) and the hump width (B) are equal. It should be noted that, in principle, the approach for $A \neq B$ would still hold as the overlapping integral could be, in the general case, numerically integrated. Nonetheless, for the sake of simplicity, we will use from now on the special case $A = B$. In this case ($A = B$), the overlapping integral yields the close form:

$$I(x,t) = 4H(t)B\operatorname{csch}(B\xi)^2[B\xi\coth(B\xi)-1]. \tag{3.4}$$

Now, proceeding with the VA methodology, we deploy the Euler-Lagrange equation for the variational parameters $\xi(t)$ and $v(t) = \dot{\xi}(t)$:

$$\frac{d}{dt}\left[\frac{\partial\mathcal{L}_a}{dv}\right] = \frac{\partial\mathcal{L}_a}{d\xi},$$

we arrive at the following effective Newton-type ODE for the soliton position:

$$\ddot{\xi} = -\frac{d}{d\xi}\left[V^{\text{eff}}(\xi)\right], \tag{3.5}$$

where the *effective* potential is given by

$$V^{\text{eff}}(\xi) = V^{\text{eff}}_{\text{MT}}(\xi) + V^{\text{eff}}_{H}(\xi) = \frac{1}{2}\Omega^2\xi^2 + 2H\operatorname{csch}(B\xi)^2[B\xi\coth(B\xi)-1], \tag{3.6}$$

containing, respectively, the effective contributions of the magnetic trap and the hump potential. Note that, contrary to the effective contribution of the magnetic trap that is identical to the original magnetic trap potential, the contribution of the hump towards the effective potential has a similar shape, but is not identical, to the hump potential itself. Figure 3 depicts the different contributions to the original potentials and their effective counterparts.

Let us now validate the fidelity of the effective ODE reduction to reproduce the bright soliton dynamics in the original PDE model. For this let us compare the corresponding orbits in phase space $(\xi,\dot{\xi})$ for typical parameter values. For the NLS model we generate bright soliton orbits by using initial conditions starting on the unstable and stable steady states $w(x)$ boosted with a velocity "kick" v_0 according to $u(x,0) = w(x)\,e^{iv_0x}$. The resulting phase space reconstruction for the original NLS model

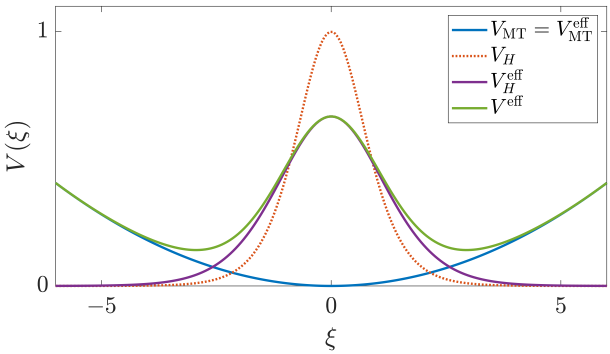

Figure 3. *(Color online) The different contributions to the original potentials and their corresponding effective counterparts. See the legend for the description of each contribution. The parameters here correspond to* $\Omega = 0.15$*,* $H = 1$*,* $B = 1$*, and* $C = B$*.*

is depicted by the thick light-colored dots/curves in panel (a) of Fig. 4. For orbits inside the separatrix (separating oscillating orbits on one side of the hump and orbits oscillating across the hump) we boost the stable steady state at the right of the hump and outside the separatrix we boost the unstable steady state centered at $x = 0$. The corresponding effective ODE orbits are depicted by the thin red lines. As we can observe from panel (a), the reduced model offers a good qualitative description of the original NLS model, however it fails at the quantitative level. After further investigation, it becomes evident that the lack of a better (quantitative) match can be accounted for by the fact of the simplicity in the soliton ansatz that we chose to use in the VA approach. In particular, we note that the shape of the phase space orbits is highly sensitive to the amplitude of the soliton. Therefore, to obtain a better quantitative match when using the reduced effective ODE model, it is essential to include more freedom on the soliton amplitude. A direct, albeit more lengthy, approach would rely in casting a VA approach with an ansatz that also includes the soliton amplitude and its chirp as variational parameters (see Sec. 25.2.1 in Ref. [13]). However, to keep our approach as simple and clean as possible and to streamline our presentation, we opt to modify our effective ODE model by introducing the amplitude of the soliton (A) as follows. To keep the overlapping integral (3.3) in closed form as in Eq. (3.4), we will assume that the (inverse) widths of the soliton and the hump are kept constant and *equal* to each other. Then, a posteriori, we adjust only the amplitude parameter by boosting the strength of the effective potential by a prefactor given by the actual soliton amplitude from the original system. To account for the soliton height, we could extract the average height of the soliton from the original NLS simulations [see panel (c) in Fig. 4]. Despite this option giving the best possible match of the effective reduced model (see Appendix A), we opt here for a completely analytical approach. Thus, we approximate the soliton height by $A + H_0$ since, as a first approximation, the height of the soliton on top of the hump will be increased by the height of the hump (H_0) itself. Thus, we simply use same shape for the effective hump potential with a prefactor $(A + H_0)/A$:

$$\widetilde{V}_H^{\mathrm{eff}}(\xi) = \frac{A + H_0}{A} V_H^{\mathrm{eff}}(\xi). \tag{3.7}$$

This improved effective model allows for (small) variations of the soliton height from the hump width B. Panel (b) in Fig. 4 shows how this improved effective model (see thin blue curves) is able to more accurately capture the phase space of the original NLS model. It is important to mention that, since we are going to be studying the stability of the soliton on top of the hill under periodic perturbations, we will be exclusively interested in the approximation of the effective model *close to the origin* ($x \approx 0$). The phase space in panel (b) evidences that the improved reduced model is quite accurate in the region $x \approx 0$.

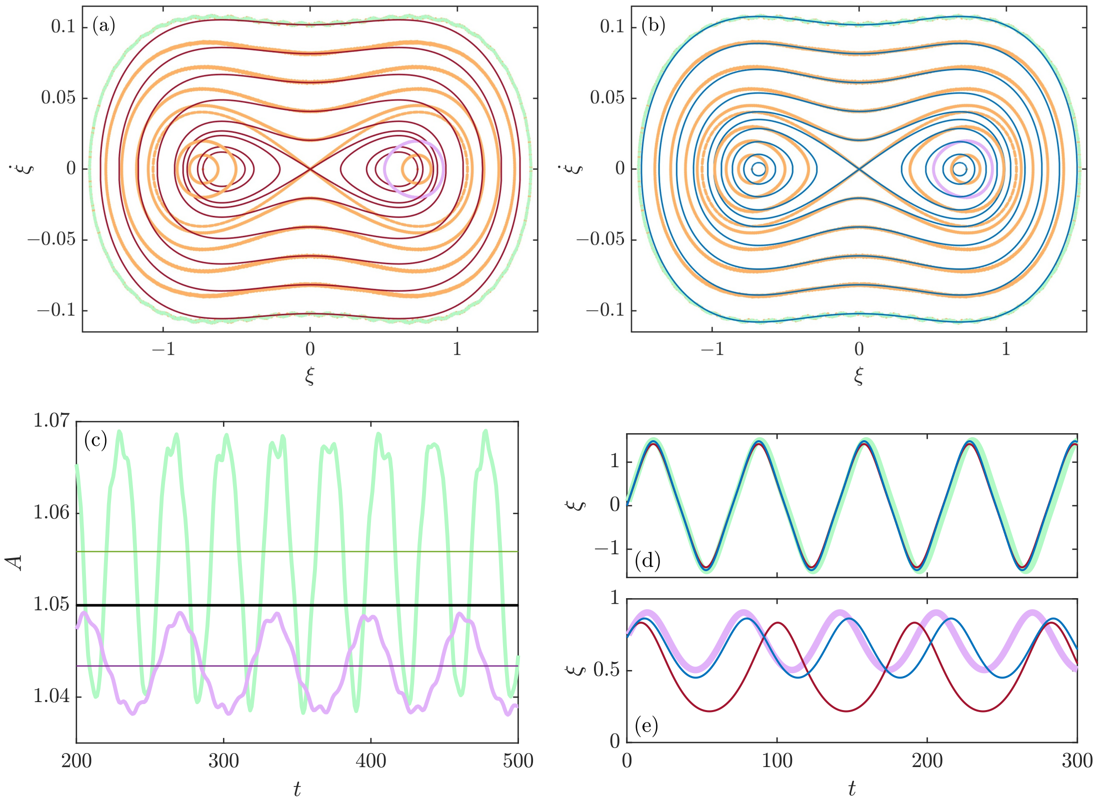

Figure 4. *(Color online) Phase space for a soliton inside a combination of harmonic trapping and a repulsive hump for* $\Omega = 0.15$*,* $H_0 = 0.05$*, and* $B = 1$*. The light orange dots depict the reconstruction of orbits from the PDE numerics while the thin blue curves depict the corresponding orbits for the reduced ODE approach. Panel (a) corresponds to the effective potential (3.6) while panel (b) corresponds to the improved effective potential (3.7) Panel (c) depicts the amplitude of the soliton for the green and purple orbits in panels (a) and (b) by least-squares fitting a of a sech profile. The green and purple horizontal lines depict the respective amplitude averages along the orbit while the black horizontal line corresponds to the estimate soliton height of* $A+H_0$*. Panels (d) and (e) depict, respectively, the green and purple orbits together with their approximation using the effective ODE models [red: original effective potential (3.6), blue: improved effective potential (3.7)].*

Therefore, unless stated otherwise, we will use from now on this improved potential for our effective ODE model of choice. Panel (c) depicts the soliton amplitude for two typical NLS orbits showing that an overall soliton amplitude approximation of $B + H_0$ is a good compromise. Finally, we depict in panels (d) and (e) representative orbits for the original NLS model and both effective models.

4. Stabilization on top of the hill: The Mathieu equation

Now that we have cast an accurate reduced model for the static hump potential, let us consider the case when the vertical shaking is on ($\Delta > 0$). In this case, our improved reduced effective model takes the form of the Newton-type Eq. (3.5) with the effective potential:

$$V^{\rm eff}(\xi) = V^{\rm eff}_{\rm MT}(\xi) + \widetilde{V}^{\rm eff}_{H}(\xi) = \frac{1}{2}\Omega^2\xi^2 + \frac{A+H_0}{A} 2H(t)\,{\rm csch}(B\xi)^2\,[B\xi\coth(B\xi) - 1], \tag{4.1}$$

where $H(t)$ given in Eq. (2.4). As we are interested in the stability of the soliton on top of the hill, for linear stability purposes it suffices to linearize the ensuing effective equations about $\xi = 0$ which yields:

$$\ddot{\xi}(t) - \left[\left(\tilde{A}\frac{8B^2}{15}H_0 - \Omega^2\right) + \tilde{A}\frac{8B^2}{15}\Delta\cos(\omega t)\right]\xi(t) = 0, \tag{4.2}$$

where $\tilde{A} \equiv (A+H_0)/A$ as argued before. Equation (4.2) has precisely the form of the Mathieu equation. Indeed, after defining $h \equiv \tilde{A}\frac{8B^2}{15\omega^2}H_0 - \frac{\Omega^2}{\omega^2}$, $\delta \equiv \tilde{A}\frac{8B^2}{15\omega^2}\Delta$, and rescaling time according to $\tau \equiv \omega t$, Eq. (4.2) reads:

$$\frac{d^2\xi(\tau)}{d\tau^2} - [h + \delta\cos(\tau)]\ \xi(\tau) = 0, \tag{4.3}$$

corresponding to the standard form of the Mathieu equation.

The Mathieu equation is a prototypical ODE with periodic coefficients that is front and center in the theory of parametric excitation, Floquet stability, and resonance tongues [41, 43, 51]. Its importance relies on the fact that many physical systems, very much like the present one, reduce to a Mathieu-type equation after linearization around an equilibrium when a periodic variation of one (or more) parameter(s) is introduced. The Kapitza (or inverted) pendulum is a classic example of this paradigm. In particular, when the pivoting point of a pendulum is vertically driven under the right conditions, the effective periodically modulated gravitational term gives rise, after linearization, to the celebrated Mathieu equation where the stability of the inverted equilibrium can be interpreted through the stability diagram (or stability tongues) of the Mathieu equation [26, 35, 51]. The Kapitza pendulum provides a concrete mechanical realization of the broader mathematical phenomenon described by Mathieu and Hill equations where the effects of the periodic parametric forcing can either destabilize or stabilize motion depending on the drive amplitude and frequency [43, 39, 50]. It is precisely this space of periodic forcing parameters that we will now explore in connection with our physical system consisting of a soliton on top of and oscillating hill. As we mentioned before, the stabilization of the bright soliton on top of the hill is tantamount to the work of Refs. [1, 37] where solitons were stabilized on top of an expulsive parabolic trap by introducing an appropriate periodic variations of, respectively, t he trap strength and the strength of the nonlinearity.

Before we use the results from the Mathieu equation, it is worth exploring the stability properties in the case when the vertical shaking is absent ($\Delta = 0$). In that case, the above linear analysis directly predicts the stability threshold from the competition of the stabilizing effects of the parabolic trap and the destabilization deriving from the hump. From the linearized Eq. (4.2) with $\Delta = 0$ this threshold directly reads as:

$$\Omega^{\text{crit}} = \sqrt{\frac{8\tilde{A}B^2}{15}H_0}. \tag{4.4}$$

This predicts that, in the static case, if $\Omega < \Omega^{\text{crit}}$ the steady state for $\xi = 0$ becomes *unstable*. Note that we write the above threshold in terms of Ω^{crit} rather than H_0^{crit} since the adjusted height $\tilde{A}$ *depends* on H_0. At any rate, the threshold (4.4) can be interpreted (i.e., inverted) in practice as a threshold for the hump height such that if $H_0 > H_0^{\text{crit}}$ the soliton on top of the static hill becomes unstable. We overlayed this threshold prediction for the soliton on top of the hill on the stability diagram of panel (g) in Fig. 2 where we used the soliton height with [$\tilde{A} = (A+H_0)/A$; see black and white dashed curve] and without ($\tilde{A} = A$; see grey dashed curve) the soliton height improvement. As it is evidenced from this figure, the improved reduced model with the adjusted soliton height is essential to obtain a good quantitative match between the original NLS model and its ODE reduction.

When the periodic forcing is present ($\delta > 0$), the Mathieu equation is well-known to exhibit stability tongues [10, 56, 34] corresponding to parameter combinations where the orbit starting at $\xi = 0$ is

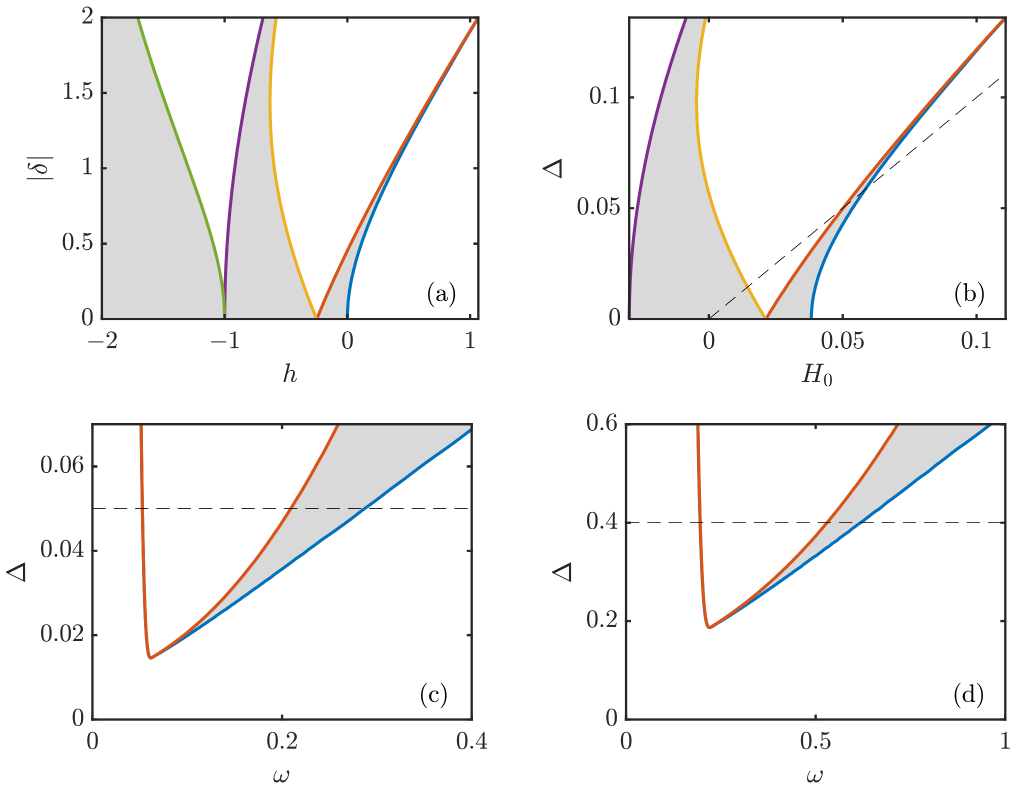

Figure 5. *(Color online) Stability regions (see gray shaded areas) for the Mathieu equation. (a) Mathieu stability regions for Eq. (4.3) as a function of h and δ. (b) Stability regions in the* (H_0, Δ) *plane for* $(\Omega, \omega, \tilde{A}) = (0.15, 0.2, A = 1)$. *(c) and (d) Stability regions in the* (ω, Δ) *plane* $(\Omega, H_0, \tilde{A}) = (0.15, 0.05, A=1)$ *and* $(\Omega, H_0, \tilde{A}) = (0.4, 0.4, A=1)$, *respectively. In all the panels, below the dashed line the periodic forcing potential never takes negative values (i.e.,* $H_0 < \Delta$*).*

completely stable. Panel (a) of Fig 5 depicts the corresponding main stability tongues in (h, δ) space. Note that the tongues are symmetric with respect to sign changes in δ. Also note that for our system of interest δ is always positive while h can be either sign depending on the combination of the system parameters. Let us now map the Mathieu stability tongues onto the original parameters of our bright soliton model under the influence of the parabolic trap and the hump's periodic vertical shaking. Panel (b) of Fig 5 depicts such stability tongues as a function of the hump nominal height H_0 and shaking amplitude Δ for the choice $(\Omega, \omega) = (0.15, 0.2)$ and without using the bright soliton amplitude improvement (i.e., $\tilde{A} = A$). On the other hand, panels (c) and (d) of Fig 5 depict the main stability tongue as a function of the periodic shaking frequency ω and amplitude Δ for, respectively, $(\Omega, H_0, \tilde{A}) = (0.15, 0.05, A=1)$ and $(\Omega, H_0, \tilde{A}) = (0.4, 0.4, A = 1)$ (namely, without the soliton height adjustment; we will introduce the height adjustment in the results below). Note that part of the second stability tongue does exist but it happens for large values of Δ where the hump potential is most of the time negative (i.e., attracting towards $\xi = 0$ for the bright soliton). In fact, to stress the fact that we want to showcase stabilization despite having a repelling hump (in the stationary case), we have drawn the dashed lines in Fig 5. We are precisely interested in the regions *below* these lines which correspond to cases where the potential hump is *never* negative (i.e., it is always repelling in its stationary form).

Now that we have access to the predictions for the parameter regions where the bright soliton would be stable according to our linear stability analysis of the reduced ODE model, we can now search for stable

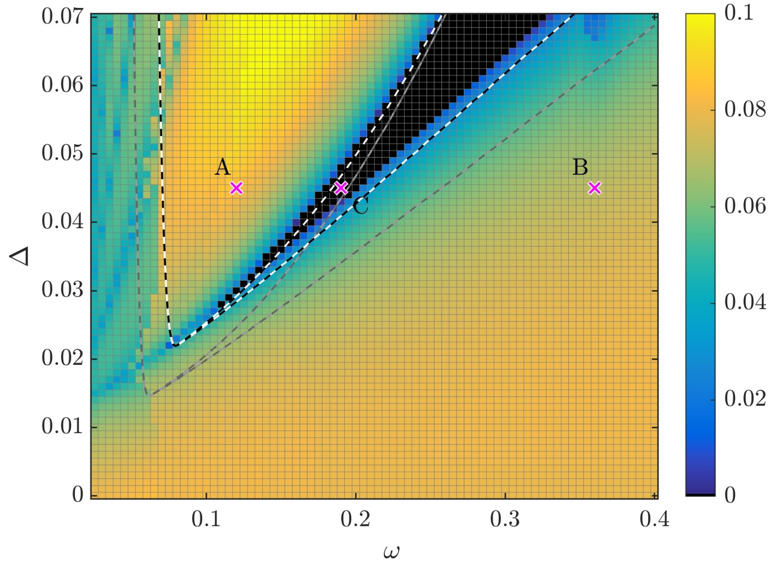

Figure 6. *(Color online) Stability diagram of the sliding mode for a bright soliton on top of the hill under a periodic perturbation of frequency* ω *and amplitude* Δ *with* $H_0 = 0.05$ *and* $\Omega = 0.15$*. Depicted is the real part of the most unstable (sliding) eigenvalue of the Floquet spectrum for the calculated periodic orbits. Darker colors correspond to less unstable conditions and black corresponds to complete stabilization. The points A (*$\omega = 0.12$*) and B (*$\omega = 0.36$*) correspond to two unstable cases while the point C (*$\omega = 0.19$*) corresponds to a stable case; all for* $\Delta = 0.045$*. The gray dashed curves depict the stability boundary regions predicted by the Mathieu equation for the original soliton amplitude of* $A = 1$ *while the black and white dashed curves correspond to the boundary regions for the improved reduced model with* $A = 1 + H_0$*.*

regions for the original NLS model. To do so we use parameter values in the window displayed in panel (c) of Fig 5. For each parameter combination we then compute the stability spectrum using Floquet theory as follows. We first, for each parameter combination, compute the steady state when the vertical shaking is absent ($\Delta = 0$) using standard fixed-point Newton iterations (as we did in Sec. 2.2). We then use this steady state solution as an initial seed for the fixed-point iteration scheme on the map generated, after one period of the forcing, on the *norm* of the solution. Namely, we find solutions to $|u(x,0)| = |u(x,T)|$ where $T = 2\pi/\omega$ is the corresponding forcing period. Subsequently, in order to use the full (complex) solution in the Floquet stability analysis, we extract the phase ϕ such that $u(x,0) = u(x,T)\, e^{i\phi}$. In this manner we obtain numerically the corresponding periodic orbit and its relative phase for each parameter combination. Once we obtain the periodic orbit with a prescribed precision (residuals below 10^{-6}), we deploy numerically a standard linear stability Floquet analysis [62, 17, 44] (after factoring out the relative phase ϕ) to extract the linear stability spectrum for each periodic orbit. Figure 6 displays the largest real part of the Floquet spectrum for $H_0 = 0.05$ and $\Omega = 0.15$ together with the Mathieu stability tongue boundaries from our dynamical reduction. Note that *complete* stabilization of the original NLS bright soliton on top of the oscillating hump is indeed possible (see region in black). The predicted stability region boundaries obtained through our reductive approach are depicted, for the case without using the soliton height improvement (i.e., $\tilde{A} = A = 1$), by the grey dashed curves. As it could have been expected, these predicted boundary regions match qualitatively the actual stability regions but fail to give a good quantitative match. In contrast, when using the effective hump potential with the improved soliton height $\tilde{A} = (A + H_0)/A$ the theoretical prediction (see black and white dashed curves) performs significantly better and allows for a decent quantitative match of the stability region.

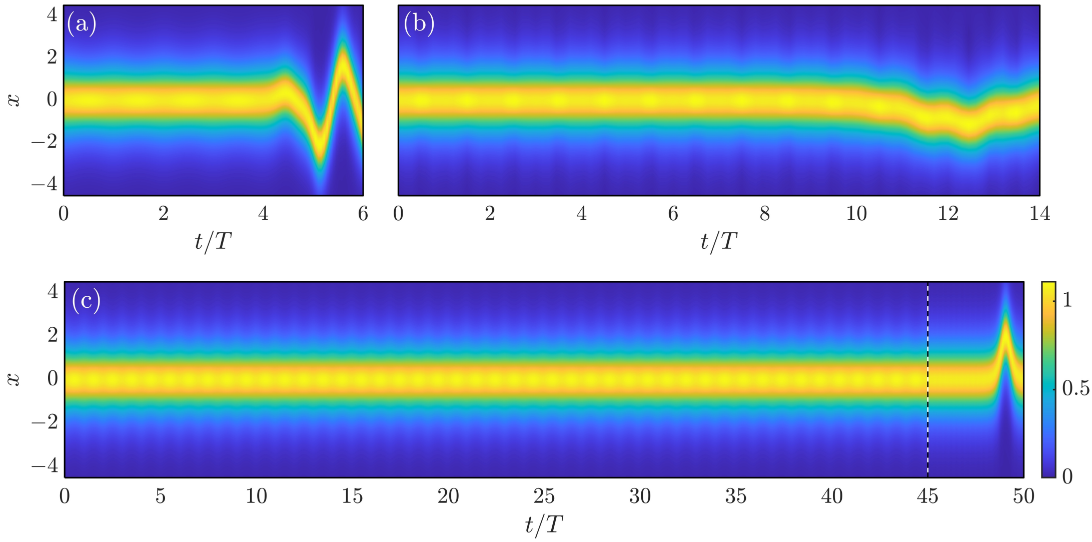

Figure 7. *(Color online) Evolution of the bright soliton under different periodic perturbations. The initial condition corresponds to the computed periodic orbit perturbed by an initial velocity "kick" imparted by multiplying the initial wave by* $\exp(iv_0x)$ *with* $v_0 = 10^{-10}$. *Panels (a), (b), and (c) corresponds, respectively, to the points A, B, and C depicted in Fig. 6. Panel (a) and (b) correspond to unstable orbits where the bright soliton rapidly slides down from the top of the hill. In contrast, panel (c) depicts a case inside the stabilization window. In this case, the bright soliton stays on top of the hill indefinitely until the vertical shaking is removed at* $t/T = 45$ *(see vertical dashed line) and, hence, the soliton rapidly slides down from the top of the hill. The panels depict the absolute value of the field as a function of time (scaled by the corresponding shaking period* $T = 2\pi/\omega$*) and space.*

To showcase the success of stabilizing the soliton on top of the hill via the periodic vertical shaking, we display typical dynamical scenarios inside and outside of the stability region. Figure 7 depicts the three different cases shown by the labeled purple crosses in Fig. 6 after the numerically computed periodic orbit is slightly perturbed by a velocity "kick" (boost) of 10^{-10}. These correspond to: unstable cases to (A) the left and to (B) the right of the stability region and (C) inside the stability region, which are displayed, respectively, in panels (a), (b), and (c) in Fig. 7. Note that, despite the fact that we used a very small velocity boost of 10^{-10}, both unstable cases destabilize rather quickly and the soliton slides down the hill after a handful of forcing periods. Also note that the destabilization for case A is faster than the one in case B as the corresponding instability (real part of the stability eigenvalue) is stronger for the former. In contrast, when choosing a parameter combination inside the stable region, the soliton is able to balance on top of the hill for long times (we have checked that it stay stable for thousands of periods; results not shown here). In fact, to showcase more vividly the stabilizing effect of the periodic shaking, for the stable case depicted panel (c) in Fig. 7, we stop the forcing after 45 periods and the bright soliton quickly slides down the hill.

In order to shed some light into the instability mechanism, we depict in Fig. 8 the Floquet spectra corresponding to the ensuing dynamical scenarios depicted in Fig. 7 (and the ones depicted in Fig. 10; see below). Note that the Floquet eigenvalues Λ are related to the stability eigenvalues λ (see Sec. 2.2) by the relation $\Lambda = e^{\lambda/T}$ where T is the period of the orbit. Floquet eigenvalues Λ lying on the unit circle ($|\Lambda| = 1$) correspond to (linearly) neutrally stable modes (depicted by small blue dots), i.e., $\mathrm{Re}(\lambda)$=0. Due to the Hamiltonian nature of the underlying PDE of the NLS model, the eigenvalues must appear in pairs (in case of being purely real or purely imaginary) or quartets (in case of being genuinely complex).

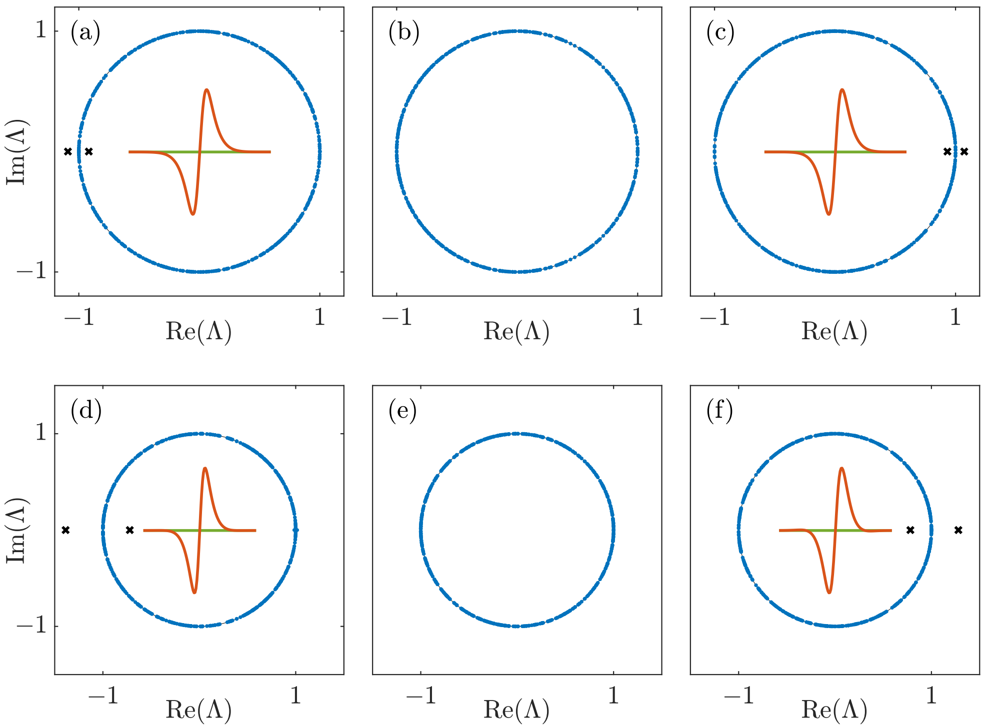

Figure 8. *(Color online) Floquet stability spectra of the periodic orbits corresponding to the points A, B, C, D, E, and F depicted in Figs. 6 and 9 (corresponding orbits depicted in Figs. 7 and 10). Non-neutral eigenpairs ($|\Lambda| \neq 1$) are depicted by the black crosses while neutral ones are depicted by small blue dots. The insets show (in case of instability) the eigenvector associated with the most unstable mode (red and green depict, respectively, the real and imaginary parts). Note that the unstable modes correspond to translational modes which are responsible of destabilizing the bright soliton from the top of the hill.*

The modes responsible for the stability or instability of the bright soliton correspond to point-spectrum eigenvalues that will lie off of the unit circle (depicted by black crosses). As it can be noticed from Fig. 8, the instabilities, when present, correspond to *real* eigenvalues indicating an exponential instability (in contrast with an oscillatory instability). This is straightforward to understand as when the soliton starts sliding down due to the instability, it will continue sliding down on the same side of the hill. We also depict in the insets the eigenmodes associated with the instability, when present, that clearly indicate that the instability is associated with the translational mode, i.e. the sliding down of the soliton from the top of the hill.

Next, to showcase that the stabilization mechanism is not exclusive for small hump potentials, we depict in Fig 9 the stability region for larger hump strengths. As the figure suggests, the stability region for larger hump strengths is greatly reduced when compared to the corresponding one for smaller hump strengths (see Fig 6). Nonetheless, as evidenced from the Floquet spectra shown in panels (d)–(f) of Fig. 8 and their corresponding dynamical evolutions shown in Fig. 10, it is indeed possible to find completely stable cases in this larger hump strength scenarios. We also note that the prediction using the improved reduced model with the adjusted soliton height (see dashed curves in the figure) is able to predict to a great extent the region of stability.

Finally, as it was the case when the periodic forcing was absent, in the general case with non-zero periodic forcing, the splitting mode might still be present. For instance, we show in Fig. 11 the Floquet spectrum [panel (a)] and it associated unstable eigenmode [panels (b) and (c)] for a case containing an

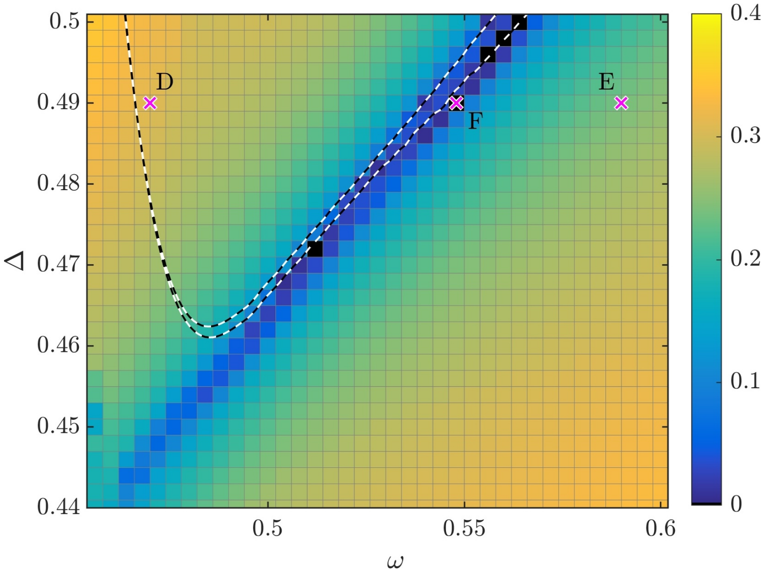

Figure 9. *(Color online) Same meaning and layout as Fig. 6 but for stronger periodic forcing and* $H_0 = 0.4$*. The points D (*$\omega = 0.475$*) and E (*$\omega = 0.588$*) correspond to two unstable cases while the point F (*$\omega = 0.548$*) corresponds to a stable case; all for* $\Delta = 0.490$*.*

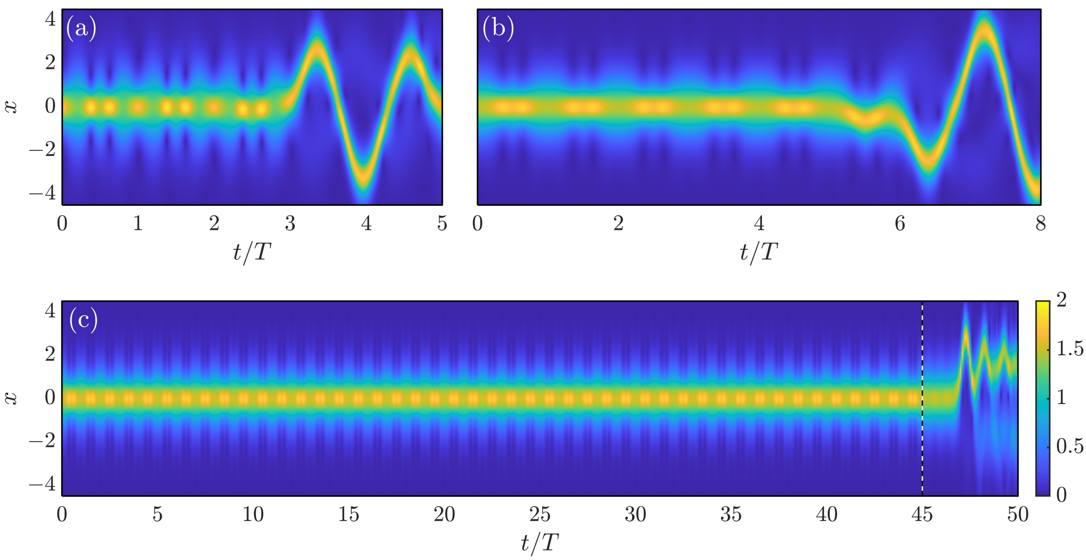

Figure 10. *(Color online) Same meaning and layout as Fig. 7 but for stronger forcing oscillations. Panels (a), (b), and (c) corresponds, respectively, to the points D, E, and F depicted in Fig. 9. Panel (a) and (b) correspond to unstable orbits where the bright soliton rapidly slides down from the top of the hill. In contrast, panel (c) depicts a case inside the stabilization window. In this case, the bright soliton stays on top of the hill indefinitely until the periodic forcing is removed at* $t/T = 45$ *(see vertical dashed line).*

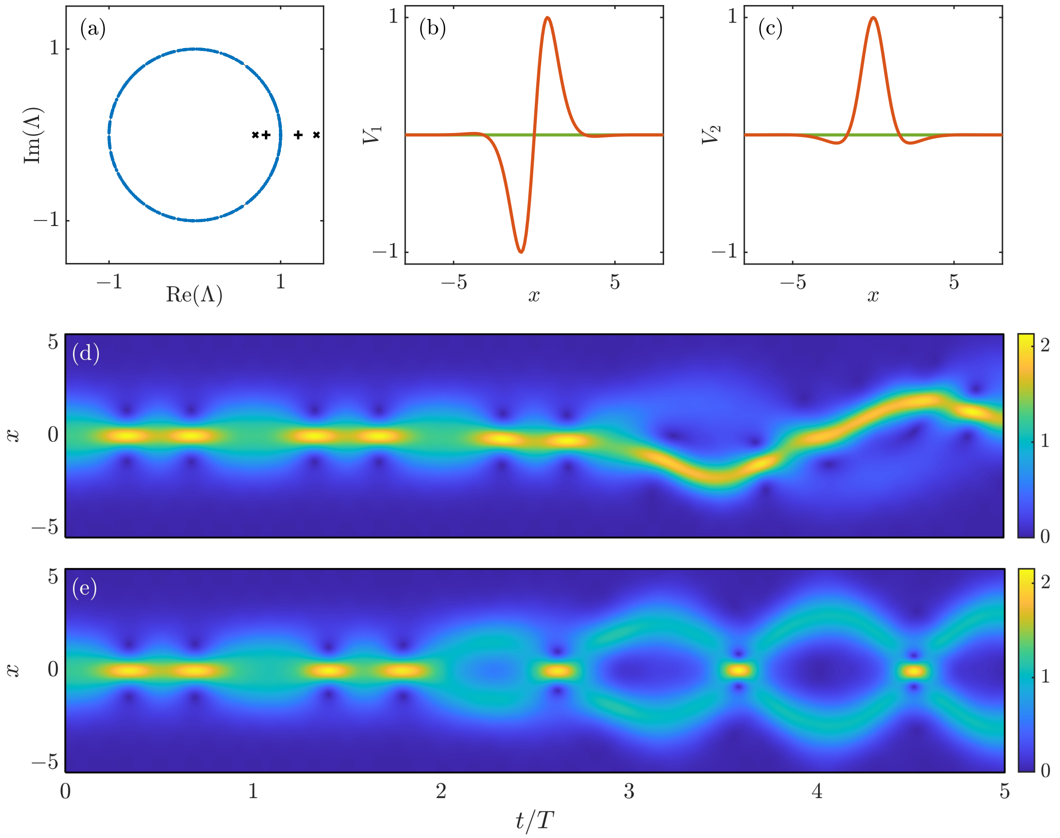

Figure 11. *(Color online) Competition of unstable modes for the periodic solution corresponding to* $H_0 = 0.4$, $\Delta = 0.5$, $\Omega = 0.4$, *and* $\omega = 0.74$. *Panel (a) depicts the Floquet spectrum while panels (b) and (c) show the eigenfunctions of the two most unstable modes [see, respectively, the cross and plus symbols in panel (a)]: (b) sliding mode and (c) splitting mode (real and imaginary parts depicted, respectively, in red and green). Panels (d) and (e) show the dynamical evolution of the unstable periodic solution slightly perturbed by, respectively, the sliding and splitting modes.*

unstable splitting mode. As we can observe, the Floquet spectrum exhibits, in addition to the *dominant* translational (sliding) mode [see panel (b)], a splitting mode [see panel (c)]. Albeit this splitting mode being less unstable that the dominant sliding mode, it is possible to excite it by perturbing the numerically computed periodic orbit with the corresponding eigenmode. Panels (d) and (e) show the ensuing dynamics when perturbing the periodic orbit by, respectively, the sliding and splitting modes. As one may observe, both modes destabilize rather quickly (after a couple of oscillations of the periodic orbit). It would be interesting to find parameter combinations that would switch the dominance between the sliding and the splitting mode. This might be possible as the stabilization provided by the periodic forcing is only designed to tame the sliding mode. Thus, it is conceivable that, for larger values of the hump strength, one would be able to completely stabilize the sliding mode (or at least make it less unstable than the splitting mode) such that the soliton on top of the hill destabilizes along the splitting mode instead of along the sliding one. Searching such a case falls outside of the scope of the current work.

5. Conclusions

In this work we construct a nonlinear-wave analogue of the famous inverted, Kapitza, pendulum which is the quintessential mechanical example exhibiting parametric stability. Our nonlinear-wave system consists of a bright soliton solution of the nonlinear Schrödinger (NLS) equation under the influence of a combined localized hump (or hill) potential and a confining parabolic trap. The hump potential is chosen to be positive and, thus, repelling when stationary. However, we show that, under appropriate vibrating hump conditions, it is possible to fully stabilize the bright soliton on top of the hill in a manner akin to the inverted pendulum stabilization via the vertical vibration of its pivoting point. To theoretically study our system, we deploy the variational approximation methodology describing the statics, stability, and dynamics of the full NLS soliton in terms of a reduced Newton-type equation on the effective soliton position. Using this reduced model, we cast the (linear) stability of the soliton on top of the vertically vibrating hill in terms of the Mathieu equation. Then, the parametric stability tongues of the Mathieu equation correspond to regions in hump parameters leading to stable periodic solutions of the soliton on top of the hill. In particular, we construct stability diagrams on the hump's oscillating frequency and amplitude that accurately predict the stability conditions of the original NLS soliton model which, in turn, are extracted by computing numerically the Floquet stability spectrum of the corresponding periodic orbits.

A complementary study to the current results would be to tackle the question of "capturing" the bright soliton on top of the hill in the first place. Namely, using appropriate control of the *horizontal* position of the hump, we have observed that it is possible, using machine learning techniques, to guide the soliton from any arbitrary position to a position close to the top of the hump. If, in addition, the control is requested to guide the soliton on top of the hump with a final small velocity, it is conceivable that, at that moment, to turn on the vertical vibration of the hump to finally stabilize the soliton on top of the hill. Doing so, one would be able to not only guide the soliton to the top of the hill by using an active control, but, once the soliton is on top of the hump with small a velocity, the active control can be turned off and replaced by a prescribed (i.e., passive) vertical vibration to fully trap the soliton on top of the hill indefinitely. We have successfully implemented examples of such a technique (results not shown here) and the corresponding results will be reported in a future publication.

Another possible avenue for further research along the lines of the current work would be to study the dynamical stabilization of dark solitons (i.e., in the case of repulsive nonlinearities) on top of localized repelling potentials under appropriate temporal vibrations. Work along these lines has been carried out in Ref. [52] where the authors studied the motion of dark solitons under periodic perturbations using adiabatic perturbation theory.

Our results may pave the ground to study parametric stabilization of localized coherent structures in other nonlinear systems. For instance, it would be interesting to explore the possibility of stabilizing localized soliton in shallow-water wave models in the presence of a vibrating hump in the bathymetry. It would also be interesting to explore the possible connections of our present work towards the stabilization of collapse of NLS bright solitons in 2D and 3D for a cubic nonlinearity [66, 45] or in 1D for higher-order nonlinearities [36, 2] under appropriate (time-) periodic forcing perturbations.

A. Appendix. Further improved reduced effective model

Figures 12 and 13 show, respectively, the phase space and stability diagrams for the further improved effective model where the prefactor of the effective hump potential is adjusted by the corresponding soliton amplitude *averaged along each individual orbit*. Note how this adjusted model provides an excellent *quantitative* description of the soliton's phase space (see Fig. 12) and, as a consequence, it is able to also give an exceptionally accurate prediction for the stability regions on the shaking hump parameters (see Fig. 13).

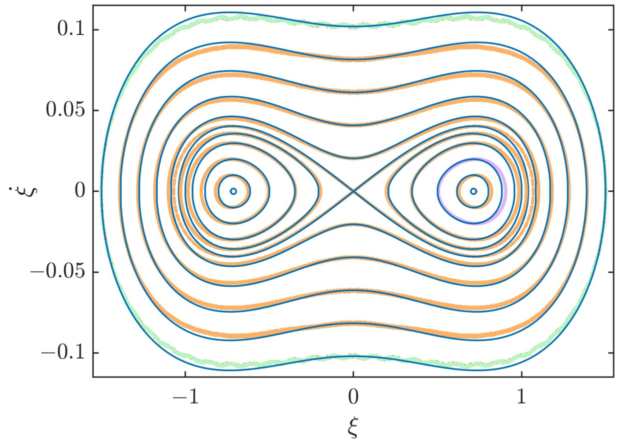

Figure 12. *(Color online) Phase space for a soliton inside a combination of harmonic trapping and a repulsive hump for $\Omega = 0.15$, $H_0 = 0.05$, and $B = 1$ when using the further improved reduced model where the prefactor on the effective hump potential is adjusted by the corresponding soliton amplitude averaged for each individual orbit. Same meaning as in panel (b) of Fig. 4.*

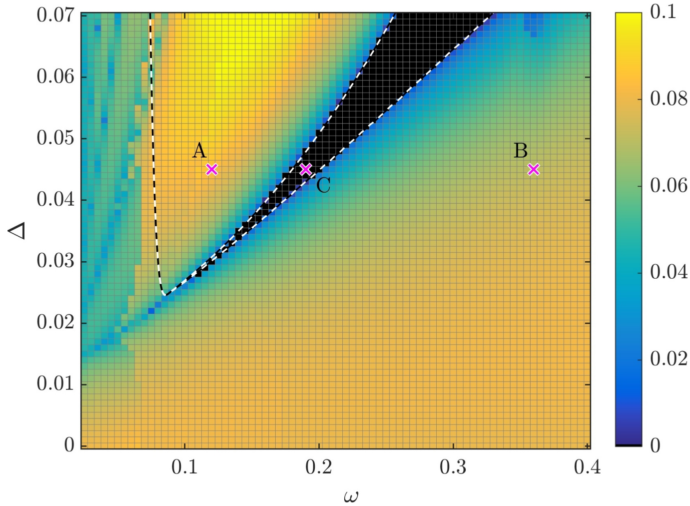

Figure 13. *(Color online) Stability diagram of the sliding mode for a bright soliton on top of the hill as in Fig. 6 but now the dashed line corresponds to the predicted stability boundary predicted using the further improved reduced model where the prefactor on the effective hump potential is adjusted by the corresponding soliton amplitude averaged for each individual orbit.*

Acknowledgments. We are grateful for stimulating discussions with Edward Finkelstein in the earliest stages of this project.

Funding Statement. This research was supported by grant NSF-PHYS-2408989.

Competing Interests. The authors declare that they have no known competing financial interests or personal relationships that could have appeared to influence the work reported in this paper.

References

[1] F.Kh. Abdullaev and R. Galimzyanov, *The dynamics of bright matter wave solitons in a quasi one-dimensional Bose-Einstein condensate with a rapidly varying trap*, Journal of Physics B: Atomic, Molecular and Optical Physics **36** (2003), no. 6, 1099.

[2] V. Achilleos, S. Diamantidis, D. J. Frantzeskakis, T. P. Horikis, N. I. Karachalios, and P. G. Kevrekidis, *Collapse for the higher-order nonlinear Schrödinger equation*, Physica D: Nonlinear Phenomena **316** (2016), 57–68.

[3] G.P. Agrawal, *Nonlinear fiber optics*, 6 ed., Academic Press, London, 2019.

[4] J.A. Blackburn, H.J.T. Smith, and N. Grønbech-Jensen, *Stability and Hopf bifurcations in an inverted pendulum*, American Journal of Physics **60** (1992), no. 10, 903–908.

[5] R.W. Boyd, D.J. Gauthier, and A.L. Gaeta, *Applications of slow light in telecommunications*, Opt. Photonics News **17** (2006), 18–23.

[6] S. Burger, K. Bongs, S. Dettmer, W. Ertmer, K. Sengstock, A. Sanpera, G.V. Shlyapnikov, and M. Lewenstein, *Dark solitons in Bose-Einstein condensates*, Physical Review Letters **83** (1999), no. 25, 5198–5201.

[7] Th. Busch and J.R. Anglin, *Motion of dark solitons in trapped Bose-Einstein condensates*, Physical Review Letters **84** (2000), no. 11, 2298–2301.

[8] E.I. Butikov, *On the dynamic stabilization of an inverted pendulum*, American Journal of Physics **69** (2001), no. 7, 755–768.

[9] ———, *An improved criterion for Kapitza's pendulum stability*, Journal of Physics A: Mathematical and Theoretical **44** (2011), no. 29, 295202.

[10] ———, *Analytical expressions for stability regions in the Ince–Strutt diagram of Mathieu equation*, American Journal of Physics **86** (2018), no. 4, 257–267.

[11] R.M. Caplan and R. Carretero-González, *Numerical stability of explicit Runge-Kutta finite-difference schemes for the nonlinear Schrödinger equation*, Applied Numerical Mathematics **71** (2013), 24–40.

[12] L.D. Carr and Y. Castin, *Dynamics of a matter-wave bright soliton in an expulsive potential*, Physical Review A **66** (2002), no. 6, 063602.

[13] R. Carretero-González, D.J. Frantzeskakis, and P.G. Kevrekidis, *Nonlinear Waves & Hamiltonian Systems: From one to many degrees of freedom, from discrete to continuum*, Oxford University Press, Oxford, 2025.

[14] R. Citro, E.G. Dalla Torre, L. D'Alessio, A. Polkovnikov, M. Babadi, T. Oka, and E. Demler, *Dynamical stability of a many-body Kapitza pendulum*, Annals of Physics **360** (2015), 694–710.

[15] F. Copie, P. Suret, and S. Randoux, *Controlled manipulation of solitons in a recirculating fiber loop using external potentials*, Physical Review Research **7** (2025), no. 4, 043232.

[16] Roberto D'Agosta and Carlo Presilla, *States without a linear counterpart in Bose-Einstein condensates*, Phys. Rev. A **65** (2002), 043609.

[17] T.F. Fairgrieve and A.D. Jepson, *O.K. Floquet multipliers*, SIAM Journal on Numerical Analysis **28** (1991), no. 5, 1446–1462, Focused paper on numerical difficulties and reliable computation of Floquet multipliers.

[18] Alexander L. Fetter, B. Jackson, and S. Stringari, *Rapid rotation of a Bose-Einstein condensate in a harmonic plus quartic trap*, Phys. Rev. A **71** (2005), 013605.

[19] D.J. Frantzeskakis, *Dark solitons in atomic Bose-Einstein condensates: From theory to experiments*, Journal of Physics A: Mathematical and Theoretical **43** (2010), no. 21, 213001.

[20] I.L. Garanovich, A.A. Sukhorukov, and Yu.S. Kivshar, *Soliton control in modulated optically-induced photonic lattices*, Optics Express **13** (2005), no. 15, 5704–5710.

[21] S.D. Hashemi and S. Mittal, *Floquet topological dissipative Kerr solitons and incommensurate frequency combs*, Nature Communications **15** (2024), 9642.

[22] Y.J. He, Boris A. Malomed, and H.Z. Wang, *Steering the motion of rotary solitons in radial lattices*, Phys. Rev. A **76** (2007), 053601.

[23] J.L. Helm, T.P. Billam, and S.A. Gardiner, *Bright matter-wave soliton collisions at narrow barriers*, Physical Review A **85** (2012), no. 5, 053621.

[24] J.K. Jang, M. Erkintalo, S. Coen, and S.G. Murdoch, *Temporal tweezing of light through the trapping and manipulation of temporal cavity solitons*, Nat. Commun. **6** (2015), 7370.

[25] Victor Kalt, Georges Sadaka, Ionut Danaila, and Frédéric Hecht, *Identification of vortices in quantum fluids: Finite element algorithms and programs*, Computer Physics Communications **284** (2023), 108606.

[26] P.L. Kapitza, *Dynamic stability of a pendulum when its point of suspension vibrates*, Soviet Physics JETP **21** (1951), 588–597.

[27] ______, *Pendulum with a vibrating suspension*, Uspekhi Fizicheskikh Nauk **44** (1951), 7–20, In Russian.

[28] Y.V. Kartashov, V.A. Vysloukh, and Ll. Torner, *Soliton shape and mobility control in optical lattices*, Progress in Optics (Emil Wolf, ed.), vol. 52, Elsevier, Amsterdam, 2009, pp. 63–148.

[29] E. Kengne, W.-M. Liu, and B.A. Malomed, *Spatiotemporal engineering of matter-wave solitons in Bose–Einstein condensates*, Physics Reports **899** (2021), 1–62.

[30] P.G. Kevrekidis, D.J. Frantzeskakis, and R. Carretero-González, *The defocusing nonlinear Schrödinger equation: From dark solitons to vortices and vortex rings*, Society for Industrial and Applied Mathematics, Philadelphia, PA, 2015.

[31] P.G. Kevrekidis, D.J. Frantzeskakis, R. Carretero-González, B.A. Malomed, G. Herring, and A.R. Bishop, *Statics, dynamics and manipulation of bright matter-wave solitons in optical lattices*, Phys. Rev. A **71** (2005), 023614.

[32] L. Khaykovich, F. Schreck, G. Ferrari, T. Bourdel, J. Cubizolles, L.D. Carr, Y. Castin, and C. Salomon, *Formation of a matter-wave bright soliton*, Science **296** (2002), no. 5571, 1290–1293.

[33] Yu.S. Kivshar and G.P. Agrawal, *Optical solitons: From fibers to photonic crystals*, Academic Press, San Diego, 2003.

[34] I. Kovacic, R.H. Rand, and S.M. Sah, *Mathieu's equation and its generalizations: Overview of stability charts and their features*, Applied Mechanics Reviews **70** (2018), no. 2, 020802.

[35] L.D. Landau and E.M. Lifshitz, *Mechanics*, 3rd ed., Course of Theoretical Physics, vol. 1, Pergamon Press, Oxford, 1976.

[36] Stefan Le Coz, Pierre Raphaël, and Jérémie Szeftel, *Self-similar blow-up profiles for slightly supercritical nonlinear Schrödinger equations*, Annales Henri Poincaré **22** (2021), no. 2, 407–450.

[37] Z.X. Liang, Z.D. Zhang, and W.M. Liu, *Dynamics of a bright soliton in Bose-Einstein condensates with time-dependent atomic scattering length in an expulsive parabolic potential*, Physical Review Letters **94** (2005), 050402.

[38] L.A. Lugiato, *Introduction to the feature section on cavity solitons: an overview*, IEEE J. Quantum Elec. **39** (2003), 193–196.

[39] W. Magnus and S. Winkler, *Hill's equation*, Interscience Publishers, New York, 1966.

[40] B.A. Malomed, *Variational methods in nonlinear fiber optics and related fields*, Progress in Optics **43** (2002), 71–193.

[41] É.L. Mathieu, *Mémoire sur le mouvement vibratoire d'une membrane de forme elliptique*, Journal de Mathématiques Pures et Appliquées **13** (1868), 137–203.

[42] G.D. McDonald, C.C.N. Kuhn, K.S. Hardman, S. Bennetts, P.J. Everitt, P.A. Altin, J.E. Debs, J.D. Close, and N.P. Robins, *Bright solitonic matter-wave interferometer*, Physical Review Letters **113** (2014), no. 1, 013002.

[43] N.W. McLachlan, *Theory and application of Mathieu functions*, Oxford University Press, Oxford, 1947.

[44] W. Mengda, X. Yonghui, and X. Ziyi, *Floquet multipliers and the stability of periodic linear differential equations: a unified algorithm and its computer realization*, Journal of Applied Analysis and Computation **13** (2023), no. 1, 575–608.

[45] Frank Merle and Pierre Raphaël, *The blow-up dynamic and upper bound on the blow-up rate for critical nonlinear Schrödinger equation*, Annals of Mathematics **161** (2005), no. 1, 157–222.

[46] Gaspar D. Montesinos, Víctor M. Pérez-García, and Humberto Michinel, *Stabilized two-dimensional vector solitons*, Phys. Rev. Lett. **92** (2004), 133901.

[47] S. Mukherjee and M.C. Rechtsman, *Observation of Floquet solitons in a topological bandgap*, Science **368** (2020), no. 6493, 856–859.

[48] ______, *Observation of unidirectional solitonlike edge states in nonlinear Floquet topological insulators*, Physical Review X **11** (2021), no. 4, 041057.

[49] ______, *Period-doubled Floquet solitons*, Optica **10** (2023), no. 10, 1310–1315.

[50] A.H. Nayfeh and D.T. Mook, *Nonlinear oscillations*, Wiley, New York, 1979.

[51] NIST Digital Library of Mathematical Functions, *Chapter 28: Mathieu functions and Hill's equation*, https://dlmf.nist.gov/28, Accessed 2026-09-09.

[52] H.E. Nistazakis, D.J. Frantzeskakis, N. Brouzakis, F.K. Diakonos, P. Schmelcher, and J. Schmiedmayer, *Time-dependent trapping of solitons in Bose-Einstein condensates*, arXiv preprint (2002), cond–mat/0211702.

[53] H.E. Nistazakis, P.G. Kevrekidis, B.A. Malomed, D.J. Frantzeskakis, and A.R. Bishop, *Targeted transfer of solitons in continua and lattices*, Phys. Rev. E **66** (2002), 015601.

[54] C.J. Pethick and H. Smith, *Bose–Einstein condensation in dilute gases*, 2 ed., Cambridge University Press, Cambridge, 2008.

[55] M.A. Porter, P.G. Kevrekidis, R. Carretero-González, and D.J. Frantzeskakis, *Dynamics and manipulation of matter-wave solitons in optical superlattices*, Phys. Lett. A **352** (2006), 210.

[56] R.H. Rand, *Lecture notes on nonlinear vibrations*, The Internet-First University Press, Ithaca, NY, 2012, Includes discussion of Mathieu equation, parametric resonance, and stability boundaries.

[57] C.J. Richards, T.J. Smart, P.H. Jones, and D. Cubero, *A microscopic Kapitza pendulum*, Scientific Reports **8** (2018), 13107.

[58] C.R. Rosberg, I.L. Garanovich, A.A. Sukhorukov, D.N. Neshev, W. Krolikowski, and Yu.S. Kivshar, *Demonstration of all-optical beam steering in modulated photonic lattices*, Optics Letters **31** (2006), no. 10, 1498–1500.

[59] J. Rossi, S. Chandramouli, R. Carretero-González, and P.G. Kevrekidis, *On the temporal tweezing of cavity solitons*, Journal of Nonlinear Mathematical Physics **31** (2024), 43.

[60] H. Sakaguchi and B.A. Malomed, *Statics, dynamics, and manipulations of bright matter-wave solitons in optical lattices*, Physical Review A **71** (2005), no. 2, 023614.

[61] V.N. Serkin, Akira Hasegawa, and T.L. Belyaeva, *Nonautonomous solitons in external potentials*, Physical Review Letters **98** (2007), no. 7, 074102.

[62] R.U. Seydel, *Practical bifurcation and stability analysis*, 3 ed., Springer, New York, 2010, Practical numerical introduction to stability and bifurcation analysis, including periodic solutions and multipliers.

[63] A. Stephenson, *XX. On induced stability*, The London, Edinburgh, and Dublin Philosophical Magazine and Journal of Science **15** (1908), no. 86, 233–236.

[64] K.E. Strecker, G.B. Partridge, A.G. Truscott, and R.G. Hulet, *Formation and propagation of matter-wave soliton trains*, Nature **417** (2002), 150–153.

[65] S. Stringari and L.P. Pitaevskii, *Bose-Einstein condensation*, Oxford University Press, Oxford, United Kingdom, 2003.

[66] Catherine Sulem and Pierre-Louis Sulem, *The nonlinear Schrödinger equation: Self-focusing and wave collapse*, Applied Mathematical Sciences, vol. 139, Springer, New York, 1999.

[67] O.J. Wales, A. Rakonjac, T.P. Billam, J.L. Helm, S.A. Gardiner, and S.L. Cornish, *Splitting and recombination of bright-solitary-matter waves*, Communications Physics **3** (2020), 51.

[68] X.-F. Zhang, Q. Yang, J.-F. Zhang, X.Z. Chen, and W.M. Liu, *Controlling soliton interactions in Bose-Einstein condensates by synchronizing the feshbach resonance and harmonic trap*, Physical Review A **77** (2008), no. 2, 023613.